Stability Analysis of a Nonlinear Distributed Control Framework for Current Sharing and Voltage Containment in DC Microgrids: The Fast Communication Scenario

Cornelia Skaga, Member, IEEE, Babak Abdolmaleki, Member, IEEE, and Gilbert Bergna-Diaz, Member, IEEE

Abstract—As renewable energy generation becomes increasingly integrated into electrical grids, there is a critical need for a paradigm shift toward control schemes that ensure safe, stable, and scalable operations. Hence, in this study, we explore the stability guarantees of a promising control proposal for cyber-physical DC microgrids (MGs), specifically designed to simultaneously achieve proportional current sharing and voltage containment within pre-specified limits. Our scalable stability result relies on singular perturbation theory to prove global exponential stability by imposing a sufficient time-scale separation at the border between the inner/decentralized and outer/distributed nested loops, and thus, ensuring that the system reaches the desired (optimal) steady state under appropriate tuning verifying some stability conditions. To prove the effectiveness of our method, our findings are supported by testing the control method in a time-domain simulation case study involving a low-voltage DC microgrid, as well as a small-signal stability analysis.

Index Terms—Converter-dominated grids, distributed control, optimal steady state operation, singular perturbation theory, stability of nonlinear systems.

I. INTRODUCTION

Driven by the increased deployment of renewable energy sources (RES) and power electronic converters, modern power grids are evolving into multi-agent converter-dominated grids with distributed communication-reliant control strategies [1], [2]. Advancements in control and management technologies have facilitated this transition, driving the development of intelligent multi-agent microgrids. These microgrids have demonstrated significant benefits in industrial applications, including power flow management in shipboard systems, marinas, and large ports with flexible loads such as electric vehicles, energy storage systems, and onshore power supplies for berthed ships [3]–[6]. Furthermore, they facilitate local energy deployment and cost-efficiency for rural electrification [7], [8]. Given the electrical characteristics of RES and modern electronic generation units and loads, DC microgrid technology has emerged as a promising solution for effectively integrating and managing RES, storage systems, and advanced electronic loads [9], [10].

From a control perspective, developing scalable and robust control schemes is crucial to ensure stability in these modern grids as they continue to expand [11]. Moreover, this growing integration of distributed (renewable) energy sources (DER) introduces challenges related to precise voltage stability and power flow management [12]. Proportional load sharing (current or power-sharing) among the distributed generation units (DGs) and stable and precise voltage regulation are therefore typically considered the two main control objectives in DC MGs [13], [14]. To ensure optimal system operations

The authors are with the Department of Electric Energy, Norwegian University of Science and Technology (NTNU), 7491 Trondheim, Norway (e-mail: cornelia.skaga@ntnu.no; babak.abdolmaleki@ntnu.no; gilbert.bergna@ntnu.no).

and control performance following these control objectives, various communication-based control strategies employing digital communication links (DCLs) in secondary controllers have been proposed. These strategies have transitioned from centralized configurations to distributed cooperative frameworks in recent years, offering enhanced scalability, reliability, flexibility, and operational efficiency [15]. When DCLs are embedded into the control framework, the microgrid is then transformed into a cyber-physical system. The distributed controller is then able to exploit the communication network to provide cooperative control actions, delivering optimal operational set-point values to the decentralized local controllers. These controllers may then restore pre-disturbance conditions, regulating the voltages, and ensure proportional current sharing while maintaining stability. However, the lack of electrical inertia in DC converter-dominated MGs makes the system particularly susceptible to transient events, highlighting the critical need for robust stability guarantees [16], [17]. To address these challenges, the Lyapunovbased large-signal stability method serves as a powerful tool for analyzing and optimizing nonlinear stability issues while offering scalable attributes facilitating stable plug-and-play conditions [16].

A. Research Gap

Recent research has introduced various distributed cooperative control frameworks for DC MGs [18]-[25], demonstrating the feasibility of achieving simultaneous current sharing and average voltage regulation. However, average voltage regulation may lead to significant deviations in individual generator voltages, potentially exceeding operational limits [9]. To overcome this limitation, [9] introduces a novel nonlinear distributed control framework. This approach ensures that all energized units contribute power proportionally to their rated capacities while dynamically operating within predefined voltage limits. The proposed controller employs a hyperbolic nonlinear saturation function at the terminals of each DG to constrain input voltage. Moreover, an anti-wind-up mechanism is implemented to maintain input voltage within safe operational boundaries. However, the nonlinear control framework was proposed without any stability proof. An almost identical control method was proposed for AC grids in [2], ensuring global asymptotic stability guarantees. The proof leveraged singular perturbation theory (SPT) accommodating scalable stability conditions under reasonable assumptions for AC grids. Specifically, the AC converters are assumed to have decentralized slow virtual synchronous machine dynamics operating at a slower time-scale than those related to the distributed communication-reliant controller. Given the natural structural differences between AC and DC grids, this assumption may arguably be counter-intuitive for DC grids. Hence it is not entirely obvious that the stability conditions provided in [2] still hold mutatis mutandis in the DC grid case in [9].

B. Contributions

This gap motivates the research presented in this paper, which aims to prove Global Exponential Stability (G.E.S.) with scalable stability guarantees when keeping similar time-scale separation assumptions to those utilized for the AC grid. Lyapunov's direct method may indeed be used to assess the stability of the case-specific system with a defined (and preferably low) number of generators admitting the structure given in [9]. That being said, the proposed control framework employs nested control loops, both inner/local and outer/distributed, thus hindering a straightforward extension of the proof to the general n-generator case and therefore making the proof difficult to scale in practice. Hence, we apply SPT to prove G.E.S. by imposing a sufficient time-scale separation at the border between the (inner and outer) nested loops, assuming slow behavior of the physical system compared to the communication [26].

We presented a preliminary stability analysis in [1], where we focused on obtaining G.E.S. proofs of the fast (communication-based) and slow (electrical and local controller) subsystems independently, albeit using SPT arguments. This paper improves the result of [1] in several directions. First, it extends the validity of the stability proof by including the dynamical interactions between both fast and slow subsystems in the stability proof via a composite Lyapunov function, hence proving G.E.S. of the full system. Second, we update the leakage function of the decentralized inner-loop controller to be a nonlinear, smooth continuous function for improved dynamical performance. Third, we have updated the simulation results to include the proposed control modifications and tested the system under realistic DC microgrid parameters that satisfy the required time-scale separation. These new case studies include various network reconfiguration events-such as load changes, generator disconnections, load failures, and transmission line outages-to highlight the plug-and-play capability of the proposed framework. Additionally, the control performance has been evaluated under assorted communication delays, further demonstrating its robustness and effectiveness under various realistic and dynamic operating conditions. Finally, we complement the study with a small-signal stability analysis, with the aim of reducing the conservativeness of the large-signal stability tuning conditions. In particular, this analysis provides some practical guidelines for reducing the fast communication rate required by the proof, and thus enhancing the applicability of the controller.

The rest of the paper is structured as follows. Section II presents the model of the electrical system and the proposed control framework. In Section III, we present the main result of this paper: a comprehensive stability proof for a closed-loop DC microgrid with a nonlinear distributed controller, that under certain tuning conditions can stabilize to a desired (optimal) steady state. Furthermore, the controller is tested in Section IV via time-domain simulations on a 4-terminals low-voltage DC microgrid to showcase the effectiveness of the method, followed by a small-signal stability analysis. Finally, section V concludes this paper.

II. SYSTEM MODELING AND CONTROL FRAMEWORK

Throughout the paper, we use the following notations: $\mathbb{R}^{n \times m}$ and \mathbb{R}^n denote a set of $n \times m$ real matrices and $n \times 1$ real vectors, respectively. $col(\cdots) \in \mathbb{R}^n$ denotes a column vector and $bcol\{\cdots\} \in \mathbb{R}^n$ denotes a column vector of vectors. $diag(\cdots) \in \mathbb{R}^{n \times n}$ denotes a diagonal matrix with scalar entries, and $\operatorname{bdiag}\{\cdots\}\in\mathbb{R}^{n\times n}$

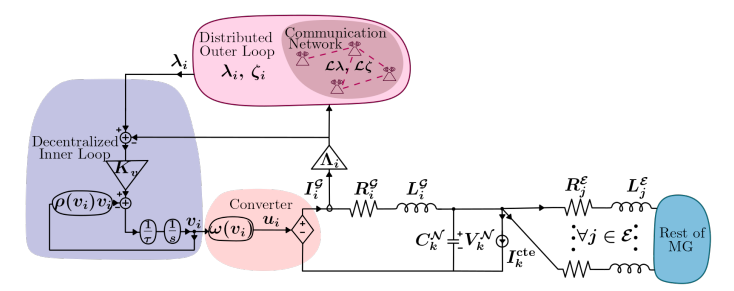


Fig. 1: DC microgrid

denotes a diagonal matrix of vectors. Given a scalar or a vector x, the value at the equilibrium point is indicated as \bar{x} .

A. Dynamical model of the Microgrid

The DC microgrid is based on the models presented in [27] and [9]. The agents are the distributed generators (DGs), located close to the power-consuming loads (ZI-loads), and are effectively interfaced with the rest of the MG through voltage-controlled converters. The converters are considered equivalent zero-order models, hence, the internal voltage controller and associated dynamics are not considered in this paper. The DGs are interconnected both electrically and via distributed communication links, forming a cyber-physical grid. Graph theory is used to establish the physical and virtual interconnections—see Appendix A in [2] for the precise definitions of the included graphs. Following the model presented in Fig. 1, the electrical dynamics for the ith DG, connected to the jth transmission line and the kth power-consuming load are presented in (1).

$$L_i^{\mathcal{G}} \dot{I}_i^{\mathcal{G}} = u_i - \sum_{k} b_{ik}^{\mathcal{G}} V_k^{\mathcal{N}} - R_i^{\mathcal{G}} I_i^{\mathcal{G}},$$
 (1a)

$$L_j^{\mathcal{E}} \dot{I}_j^{\mathcal{E}} = -\sum_{i} b_{jk}^{\mathcal{E}} V_k^{\mathcal{N}} - R_j^{\mathcal{E}} I_j^{\mathcal{E}}, \tag{1b}$$

$$L_{i}^{\mathcal{G}}\dot{I}_{i}^{\mathcal{G}} = u_{i} - \sum_{k} b_{ik}^{\mathcal{G}} V_{k}^{\mathcal{N}} - R_{i}^{\mathcal{G}} I_{i}^{\mathcal{G}}, \tag{1a}$$

$$L_{j}^{\mathcal{E}}\dot{I}_{j}^{\mathcal{E}} = -\sum_{k} b_{jk}^{\mathcal{E}} V_{k}^{\mathcal{N}} - R_{j}^{\mathcal{E}} I_{j}^{\mathcal{E}}, \tag{1b}$$

$$C_{k}^{\mathcal{N}}\dot{V}_{k}^{\mathcal{N}} = \sum_{j} b_{kj}^{\mathcal{E}} I_{j}^{\mathcal{E}} + \sum_{i} b_{ki}^{\mathcal{G}} I_{i}^{\mathcal{G}} - G_{k}^{\text{cte}} V_{k}^{\mathcal{N}} - I_{k}^{\text{cte}}, \tag{1c}$$

where $L_i^{\mathcal{G}}$, $R_i^{\mathcal{G}}$, $I_i^{\mathcal{G}}$, and u_i are respectively the inductance, resistance, current, and voltage of the *i*th DG. $L_j^{\mathcal{E}}$, $R_j^{\mathcal{E}}$, and $I_j^{\mathcal{E}}$ are respectively the inductance, resistance, and current of the jth transmission line. $C_k^{\mathcal{N}},\,V_k^{\mathcal{N}},\,G_k^{\mathrm{cte}}$ and I_k^{cte} are respectively the shunt capacitance, its voltage, the constant conductance, and constant current of the kth power-consuming load. The elements $b_{ik}^{\mathcal{G}}$ and $b_{jk}^{\mathcal{E}}$ correspond to the incidence matrices, characterizing arbitrary current flows within the network. When current flows from the ith generator to the kth load, the matrix element $b_{ik}^{\mathcal{G}}$ is set to 1. Conversely, for an opposite power flow, $b_{ik}^{\mathcal{G}}$ is assigned -1. However, $b_{ik}^{\mathcal{G}} = -1$ is not considered in this study as we treat the DGs as power injection components. In the absence of current exchange between the ith generator and the kth load, $b_{ik}^{\mathcal{G}}$ is set to 0. Similarly, the matrix element $b_{kj}^{\mathcal{E}}$ characterizes current flows between loads interconnected by transmission lines.

In Section II.C in [9], the modeling of the distributed control layer is presented, exploiting communication between neighboring DGs to ensure consensus properties and subsequently proportional current sharing. In summary, the distributed controller is derived by means of the Lagrange multiplier method, where it ensures that the system stabilizes at an equilibrium which is the argument that minimizes a cost function. More precisely, the cost function was

chosen to achieve current sharing in a steady state. The distributed control layer, together with the local current regulator aims to ensure the two control objectives simultaneously: voltage containment and proportional current sharing. The distributed optimizer relies on obtaining the rated current from each DG. Hence, the output of the physical network is then defined as the ratio of the DGs actual current to its rated current: $\Lambda_i I_i^{\mathcal{G}} = I_i^{\mathcal{G}} / I_i^{\text{rated}}, \forall i \in \mathcal{G}$. For the *i*th DG, the control scheme is defined as follows:

$$u_i = V_i^{\text{set}} = \omega(v_i) = V^* + \Delta \tanh(v_i/\Delta), \tag{2a}$$

$$\tau_i \dot{v}_i = -\rho(v_i) v_i + k_V (\lambda_i - \Lambda_i I_i^{\mathcal{G}}), \tag{2b}$$

$$\tau_i^p \dot{\lambda}_i = \Lambda_i I_i^{\mathcal{G}} - \lambda_i - \sum_{j \in N_i} [a_{ij} (\zeta_i - \zeta_j) - k a_{ij} (\lambda_j - \lambda_i)], \tag{2c}$$

$$\tau_i^d \dot{\zeta}_i = \sum_{j \in N_i} a_{ij} (\lambda_i - \lambda_j), \tag{2d}$$

$$\rho(v_i) = \alpha(1 + 0.5[\tanh(b(v_i - v_{pos})) - \tanh(b(v_i - v_{neg}))]), \quad (2e)$$

The distributed control framework depends on three controller states where λ_i and ζ_i are the communicated states of the cyber network with respective time constants τ_i^p and τ_i^d . v_i is the decentralized controller state with associated time constant τ_i , and associated controller gain, k_v , tuning the velocity for the integrator. In [9] k_v is treated as the fixed value V^* . However, we find it convenient for the stability proof to treat it as a tunable parameter here—see Section III-C for more details. u_i is the control actuator, constructed by the nonlinear function $\omega(v_i)$ implemented for voltage containment. $\tanh(\cdot)$ is a hyperbolic tangent function used to saturate the argument of ω if v_i exceeds the predefined limits. $V^* = \frac{1}{2}(V_{\min} + V_{\max})$ is the central point within the safe voltage range, and $\Delta = \frac{1}{2}(V_{\text{max}} - V_{\text{min}})$ is the maximum allowed deviation from V^* . $tanh(\cdot)$ is also used in $\rho(v_i)$ as a nonlinear leakage expression operating as an anti-wind-up function when we reach voltage saturation under the given arguments; $v_{\rm pos} = \Delta \tanh^{-1}[(v_{\rm max}$ $v_{\rm tol} - V^*)/\Delta$ and $v_{\rm neg} = \Delta \tanh^{-1}[(v_{\rm min} + v_{\rm tol} - V^*)/\Delta]$, where $v_{\rm tol}$ is the saturation tolerance, α is the leakage coefficient scaling the upper bound value of the leakage and b is implemented to scale the steepness of the curve. Finally, a_{ij} is the adjacency matrix element, describing the communicating DGs where N_i is the set of the neighboring DGs in the cyber layer, and k is a positive gain.

III. SYSTEM STEADY STATE AND STABILITY ASSESSMENT

We start by expressing the system dynamics (1)-(2) in the compact form:

$$L^{\mathcal{G}}\dot{I}^{\mathcal{G}} = \omega(v) - \beta^{\mathcal{G}}V^{\mathcal{N}} - R^{\mathcal{G}}I^{\mathcal{G}}, \tag{3a}$$

$$L^{\mathcal{E}}\dot{I}^{\mathcal{E}} = -\beta^{\mathcal{E}}V^{\mathcal{N}} - R^{\mathcal{E}}I^{\mathcal{E}}, \tag{3b}$$

$$C^{\mathcal{N}}\dot{V}^{\mathcal{N}} = \beta^{\mathcal{E}^{\top}}I^{\mathcal{E}} + \beta^{\mathcal{G}^{\top}}I^{\mathcal{G}} - G^{\text{cte}}V^{\mathcal{N}} - I^{\text{cte}}, \tag{3c}$$

$$C^{\mathcal{N}}\dot{V}^{\mathcal{N}} = \beta^{\mathcal{E}^{\top}}I^{\mathcal{E}} + \beta^{\mathcal{G}^{\top}}I^{\mathcal{G}} - G^{\text{cte}}V^{\mathcal{N}} - I^{\text{cte}}, \tag{3c}$$

$$\tau \dot{v} = -\rho(v)v + \mathcal{K}_V(\lambda - \Lambda I^{\mathcal{G}}), \tag{3d}$$

$$\tau_p \dot{\lambda} = \Lambda I^{\mathcal{G}} - \lambda - \mathcal{L}\zeta - k\mathcal{L}\lambda, \tag{3e}$$

$$\tau_d \dot{\zeta} = \mathcal{L}\lambda,$$
 (3f)

with $L^{\mathcal{G}} = \operatorname{diag}(L_i^{\mathcal{G}}) \in \mathbb{R}^{n_i \times n_i}$, $I^{\mathcal{G}} = \operatorname{col}(I_i^{\mathcal{G}}) \in \mathbb{R}^{n_i}$, $R^{\mathcal{G}} = \operatorname{diag}(R_i^{\mathcal{G}}) \in \mathbb{R}^{n_i \times n_i}$, $\omega(v) = \operatorname{col}(\omega(v_i)) \in \mathbb{R}^{n_i}$, $\beta^{\mathcal{G}} = [b_{ik}^{\mathcal{G}}] \in \mathbb{R}^{n_i \times n_k}$. $L^{\mathcal{E}} = \operatorname{diag}(L_i^{\mathcal{E}}) \in \mathbb{R}^{n_j \times n_j}$, $I^{\mathcal{E}} = \operatorname{col}(I_j^{\mathcal{E}}) \in \mathbb{R}^{n_j}$, $R^{\mathcal{E}} = \operatorname{diag}(R_j^{\mathcal{E}}) \in \mathbb{R}^{n_j \times n_j}$, $\beta^{\mathcal{E}} = [b_{jk}^{\mathcal{E}}] \in \mathbb{R}^{n_j \times n_k}$. $C^{\mathcal{N}} = \operatorname{diag}(C_k^{\mathcal{N}}) \in \mathbb{R}^{n_k \times n_k}$, $V^{\mathcal{N}} = \operatorname{col}(V_k^{\mathcal{N}}) \in \mathbb{R}^{n_k}$, $C^{\text{Cte}} = \operatorname{diag}(C_k^{\text{Cte}}) \in \mathbb{R}^{n_k \times n_k}$, where $I^{\text{cte}} = \text{col}(I_k^{\text{cte}}) \in \mathbb{R}^{n_k}, \quad v = \text{col}(v_i^c) \in \mathbb{R}^{n_i}, \quad \tau = \text{diag}(\tau_i) \in \mathbb{R}^{n_i \times n_i}, \\ \rho(v) = \text{diag}(\rho(v_i)) \in \mathbb{R}^{n_i \times n_i}, \quad \mathcal{K}_v = \text{diag}(\mathbf{k}_v) \in \mathbb{R}^{n_i \times n_i},$

$$\begin{split} \lambda &= \operatorname{col}(\lambda_i) \in \mathbb{R}^{n_i}, \ \Lambda = \operatorname{diag}(1/I_{\operatorname{rated}}^{\mathcal{G}}) \in \mathbb{R}^{n_i \times n_i}, \ \zeta = \operatorname{col}(\zeta_i) \in \mathbb{R}^{n_i}, \\ \tau_p &= \operatorname{diag}(\tau_i^p) \ \in \ \mathbb{R}^{n_i \times n_i}, \ \tau_d \ = \ \operatorname{diag}(\tau_{di}) \ \in \ \mathbb{R}^{n_i \times n_i}. \ \text{Finally,} \end{split}$$
 $\mathcal{L} = [l_{ij}] \in \mathbb{R}^{n_i \times n_i}$ is the *Laplacian* matrix, containing the consensus properties of the strongly connected communication network.

A. Equilibrium Analysis

Lemma 1. (Steady State). We derive the steady state equations of (3) by expressing $\dot{x} = 0_n$ for all the states. Hence, any steady state needs to satisfy

$$0 = f(\bar{I}^{\mathcal{G}}, \bar{I}^{\mathcal{E}}, \bar{V}^{\mathcal{N}}, \bar{v}),
0 = g(\bar{v}, \bar{\lambda}, \bar{\zeta}, \bar{I}^{\mathcal{G}}),$$

where $f(\cdot)$ contains the dynamics of the electrical system and the decentralized current regulator in (3a)-(3d), and $g(\cdot)$ contains the dynamics of the distributed control system (3e)-(3f).

Leveraging the property of the Laplacian matrix where $\mathcal{L}1_n = 0$, the steady state operations of (3f) leads to all the DGs cooperatively agreeing upon one consensus value for the communicated state variable $\bar{\lambda} = \lambda_s 1_{n_i}$ where λ_s is the singular consensus value and $1_{n_i} = \operatorname{col}(1) \in \mathbb{R}^{n_i}$. When considering steady state operation of (3d) without saturated voltages, and thereby inactivated leakage function $\rho(\bar{v})$, $\Lambda \bar{I}^{\mathcal{G}}$ is forced equal to $\bar{\lambda}$. Subsequently, steady state operations provide consensus among the DGs in regards to the other communicated value when (3e) converge to the equilibrium and $\zeta = \zeta_s 1_{n_s}$, where ζ_s is the singular consensus value. The steady state of the electrical network (3a)-(3c) is consequently uniquely defined.

Remark 1. (Optimal Steady State) Subsequent to Lemma 1 our system attains optimal operations when saturation is avoided, simultaneously ensuring proportional current sharing and voltage containment when $\Lambda \bar{I}^{\mathcal{G}} = \bar{\lambda}$ at the equilibrium.

In Section II.D in [9] the optimal steady state operation is defined from the solution of the Distributed Multi-Variable Optimization problem employing Lagrangian multipliers and Karush-Kuhn-Tucker (KKT) conditions. It is proven that the system reaches its optimal steady state when $\Lambda \bar{I}^{\mathcal{G}} = \bar{\lambda}$. This condition is satisfied when all DGs collaboratively determine the optimal set-point value $\bar{\lambda}$, ensuring proportional current sharing at the equilibrium. However, in the case of voltage saturation, the MG is steered to a sub-optimal steady state due to the presence of the leakage function in (3d), diminishing optimal proportional current sharing at the equilibrium.

B. Stability Assessment

We aim to prove that the equilibrium of (3) is globally exponentially stable using singular perturbation theory. First, we reduce the order of the system using similar arguments to those used in [2]. This simplifying assumption is detailed in the following lines.

1) Model Reduction: As the control parameters are tunable, we make the following assumption for the time constants τ, τ_n, τ_d .

Assumption 1. $\tau_p \ll \tau_d \ll \tau$ with $\varepsilon = \tau_d$ when τ is the fastest time constant of the slow system.

Under Assumption 1, the term $\tau_p \dot{\lambda}$ can be neglected. Hence, we eliminate the left-hand side of equation (3e) and consider $\lambda = K_1 \Lambda I^{\mathcal{G}} - K_1 \mathcal{L}\zeta$, with $K_1 \triangleq [\mathbb{I} + k\mathcal{L}]^{-1} > 0$. Under Assumption 1, the right side of (3f) being a function of λ results in some added damping in the estimator state ζ coordinate. Consequently, the system in (3) is reduced to

$$L^{\mathcal{G}}\dot{I}^{\mathcal{G}} = \omega(v) - \beta^{\mathcal{G}}V^{\mathcal{N}} - R^{\mathcal{G}}I^{\mathcal{G}},\tag{5a}$$

$$L^{\mathcal{E}}\dot{I}^{\mathcal{E}} = -\beta^{\mathcal{E}}V^{\mathcal{N}} - R^{\mathcal{E}}I^{\mathcal{E}},\tag{5b}$$

$$C^{\mathcal{N}}\dot{V}^{\mathcal{N}} = \beta^{\mathcal{E}^{\top}}I^{\mathcal{E}} + \beta^{\mathcal{G}^{\top}}I^{\mathcal{G}} - G^{\text{cte}}V^{\mathcal{N}} - I_{c}^{\text{cte}}, \tag{5c}$$

$$\tau\dot{v}\!=\!-\rho(v)v\!+\!\mathcal{K}_v(K_1\Lambda I^{\mathcal{G}}\!-\!K_1\mathcal{L}\zeta\!-\!\Lambda I^{\mathcal{G}})\!-\!\mathcal{B}(v\!-\!v^*), \ \ (\mathsf{5d})$$

$$\varepsilon \dot{\zeta} = \mathcal{L} K_1 \Lambda I^{\mathcal{G}} - \mathcal{L} K_1 \mathcal{L} \zeta. \tag{5e}$$

Additionally, a *small* permanent leakage term $\mathcal{B} = \operatorname{diag}[b_i] \in \mathbb{R}^{n_i \times n_i}$ is introduced to the controller to add dissipation with respect to the regulator state v when the voltages are within limits, and $\rho(v)$ will have zero value. v^* is the constant estimated value of v in steady state; \bar{v} , for the ideal nominal operating point.

2) Time-scale Separation and Singular Perturbation Analysis: We apply singular perturbation theory to obtain *scalable* stability conditions for the system in (5). We use time-scale separation, where (5a)-(5d) is considered as the slow dynamics, and (5e) is considered the fast dynamics under Assumption 1. Thus, we define the two time-separated systems as

$$\dot{x} = f(x,\zeta)$$
 and $\varepsilon \dot{z} = g(x,\zeta)$,

where $x = [I^{\mathcal{G}}, I^{\mathcal{E}}, V^{\mathcal{N}}, v]^{\top 1}$.

Theorem 1. (Exponential Stability). Consider that the system in (3), (5) satisfies the following matrix inequalities,

$$\mathcal{B} \ge \mathcal{B}^* \ge H^\top R^{\mathcal{G}-1} H \omega'(v),$$

where $H \triangleq -\frac{1}{2}[\mathbb{I} + \Lambda h^{\top}]$, $h \triangleq \mathcal{K}_v(K_1 - K_1\mathcal{L}K_2 - \mathbb{I})$, $K_1 \triangleq [\mathbb{I} + k\mathcal{L}]^{-1}$, $K_2 \triangleq [\mathcal{L}K_1\mathcal{L}]^{-1}\mathcal{L}K_1$, and \mathcal{B}^* is the maximum eigenvalue of $H^{\top}R^{\mathcal{G}-1}H\omega'_{\max}$. Then, there exists $\varepsilon^* > 0$ such that for all $\tau_d < \varepsilon < \varepsilon^*$ the system in (3), (5) is globally exponentially stable.

Proof. We consider $\varepsilon = \tau_d$ to be very small such that the velocity of $\zeta \propto (1/\varepsilon)$ behaves instantaneously fast where ζ rapidly converges to the root of $0_n = \mathcal{L}K_1\Lambda I^{\mathcal{G}} - \mathcal{L}K_1\mathcal{L}\zeta$. Hence, the fast system in (5e) quickly achieves a *quasi-steady state* where $\zeta = [\mathcal{L}K_1\mathcal{L}]^{-1}\mathcal{L}K_1\Lambda I^{\mathcal{G}}$. For simplicity we define $K_2 \triangleq [\mathcal{L}K_1\mathcal{L}]^{-1}\mathcal{L}K_1$. To facilitate applying Lyapunov theory, let the states be incrementally expressed as: $\tilde{x} = x - \bar{x}$ and $\tilde{y} = y - \bar{y}$. Since the monotonic functions $\omega(v)$ and $\rho(v)v$ are element-wise strictly increasing in v, it is useful to define

$$\Omega(\tilde{v}) \triangleq \omega(v) - \omega(\bar{v}), \text{ and } \Gamma(\tilde{v}) \triangleq \rho(v)v - \rho(\bar{v})\bar{v}.$$

Let \tilde{y} be the error between the actual fast dynamics, $\tilde{\zeta}$, and the quasi-steady states $h(\tilde{x})$; i.e., $\tilde{y} = \tilde{\zeta} - h(\tilde{x})$ where $h(\tilde{x}) = K_2 \Lambda \tilde{I}^{\mathcal{G}}$. The system in (5) may then be expressed as a singular perturbation problem partitioned into the reduced system (6) and the boundarylayer system (7), divided under the stretched time-scale $\mathbf{t} = (t/\varepsilon)$ where t is the time when $\varepsilon \approx 0$. The slow dynamics will then instantaneously achieve a quasi-steady state such that $y \approx 0$ in the reduced system. Subsequently, the slow states entering the boundary layer system are considered constants.

For compactness, we_define the physical state vector $\tilde{\hat{x}} \triangleq \begin{bmatrix} \tilde{I}^{\mathcal{G}} & \tilde{I}^{\mathcal{E}} & \tilde{V}^{\mathcal{N}} \end{bmatrix}^{\top}$; the physical resistance matrix $\mathcal{P}_x \triangleq \operatorname{bdiag}\{R^{\mathcal{G}}, R^{\mathcal{E}}, G^{\operatorname{cte}}\} \succ 0$; the physical inertia matrix $\mathcal{Q}_x \triangleq \operatorname{bdiag}\{L^{\mathcal{G}}, L^{\mathcal{E}}, C^{\mathcal{N}}\} \succ 0$ containing inductance and capacitance of the physical system; $h = \mathcal{K}_v(K_1 - K_1 \mathcal{L} K_2 - \mathbb{I})$; and the interconnection matrix

$$\mathcal{J}_{x} \triangleq \begin{bmatrix} \mathbf{0}_{n_{i} \times n_{i}} & \mathbf{0}_{n_{i} \times n_{j}} & -\beta^{\mathcal{G}} \\ \mathbf{0}_{n_{j} \times n_{i}} & \mathbf{0}_{n_{j} \times n_{j}} & -\beta^{\mathcal{E}} \\ \beta^{\mathcal{G} \top} & \beta^{\mathcal{E} \top} & \mathbf{0}_{n_{k} \times n_{k}} \end{bmatrix}; \quad \text{and with}$$

$$\kappa_{1} \triangleq \begin{bmatrix} \mathbf{1}_{n_{i} \times n_{i}} & \mathbf{0}_{n_{i} \times n_{j}} & \mathbf{0}_{n_{i} \times n_{k}} \\ \mathbf{0}_{n_{j} \times n_{i}} & \mathbf{0}_{n_{j} \times n_{j}} & \mathbf{0}_{n_{j} \times n_{k}} \\ \mathbf{0}_{n_{k} \times n_{i}} & \mathbf{0}_{n_{k} \times n_{j}} & \mathbf{0}_{n_{k} \times n_{k}} \end{bmatrix}.$$

The reduced system is then expressed in compact form as

$$f(\tilde{x}, h(\tilde{x})) : \begin{cases} Q_x \dot{\tilde{x}} = (\mathcal{J}_x - \mathcal{P}_x) \hat{x} + \kappa_1 \Omega(\tilde{v}) \\ \dot{\tau} \dot{\tilde{v}} = -\Gamma(\tilde{v}) + h \Lambda \kappa_1^\top \hat{x} - \beta \tilde{v} \end{cases}$$
(6)

For the boundary layer system, we define the cyber resistance matrix $\mathcal{P}_y \triangleq \mathcal{L}K_1\mathcal{L} \succ 0$, such that the boundary layer is expressed by

$$g(\tilde{x}, y + h(\tilde{x})) : \left\{ \partial \tilde{y} / \partial \mathbf{t} = -\mathcal{P}_y \tilde{y} \right\}$$
 (7)

Two Lyapunov candidates for the reduced system (6) and boundary layer system (7) are then given below.

$$V_s(\tilde{\hat{x}}, \tilde{v}) = \frac{1}{2} \tilde{\hat{x}}^\top \mathcal{Q}_x \tilde{\hat{x}} + \int_0^v \Omega^\top(\sigma) \tau d\sigma \ge 0,$$

$$W_f(\tilde{y}) = \frac{1}{2} \tilde{y}^\top \tilde{y} \ge 0.$$

Their time-derivative along the trajectories of the two systems are

$$\dot{V}_{s}(\tilde{x}) = \nabla^{\top} V_{s}(\tilde{x}) \dot{\tilde{x}} = \tilde{\hat{x}}^{\top} \mathcal{Q}_{x} \dot{\tilde{x}} + \Omega^{\top}(\tilde{v}) \tau \dot{\tilde{v}} \leq 0, \tag{9a}$$

$$\frac{\partial W_f(\tilde{y})}{\partial \mathbf{t}} = \nabla^\top W_f(\tilde{y}) \dot{\tilde{y}} = \tilde{y}^\top \frac{\partial \tilde{y}}{\partial \mathbf{t}} \le 0. \tag{9b}$$

Inserting system dynamics (6) into (9) gives

$$\begin{split} \dot{V}_{s}(\tilde{x}) &= -\tilde{\hat{x}}^{\top} \mathcal{P}_{x} \tilde{\hat{x}} + \tilde{\hat{x}}^{\top} \kappa_{1} \Omega(\tilde{v}) - \Omega^{\top}(\tilde{v}) \Gamma(\tilde{v}) \\ &- \Omega^{\top}(\tilde{v}) \beta \tilde{v} + \Omega^{\top}(\tilde{v}) h \Lambda \kappa_{1}^{\top} \tilde{\hat{x}} \\ &= -(x - \bar{x})^{\top} [\mathcal{M}_{x}(x) - \mathcal{M}_{x}(\bar{x})] - \Omega(\tilde{v})^{\top} \Gamma(\tilde{v}), \end{split} \tag{10a}$$

$$\frac{\partial W_f(\tilde{y})}{\partial \mathbf{t}} = -\tilde{y}^{\mathsf{T}} \mathcal{P}_y \tilde{y},\tag{10b}$$

with
$$x \triangleq \begin{bmatrix} \hat{x} \\ v \end{bmatrix}$$
, and $\mathcal{M}_x(x) \triangleq \begin{bmatrix} \mathcal{P}_x \hat{x} - \kappa_1 [\mathbb{I} + \Lambda h^\top] \omega(v) \\ \mathcal{B}\omega(v) \end{bmatrix}$.

Both $\Omega(\tilde{v})$ and $\Gamma(\tilde{v})$ are element-wise monotonically increasing with respect to \tilde{v} . Hence, the last term in (10a) becomes negative; i.e., $-\Omega(\tilde{v})^{\top}\Gamma(\tilde{v}) \leq 0.$

The first term of (10a) is negative definite if $\mathcal{M}_x(x)$ is strictly monotonic; that is,

$$\tilde{x}^{\top}(\mathcal{M}_x(x) - \mathcal{M}_x(\bar{x})) \ge 0 \Leftrightarrow \frac{1}{2} \left[\frac{\partial \mathcal{M}_x(x)}{\partial x} + \frac{\partial \mathcal{M}_x(x)}{\partial x}^{\top} \right] \ge 0.$$

Computing the symmetric part of $\frac{\partial \mathcal{M}_x(x)}{\partial x}$ required for the above condition gives:

$$\left. \frac{\partial \mathcal{M}_x}{\partial x} \right|_{\text{sym}} = \begin{bmatrix} R^{\mathcal{G}} & 0 & 0 & H\omega'(v) \\ 0 & R^{\mathcal{E}} & 0 & 0 \\ 0 & 0 & G^{\text{cte}} & 0 \\ \omega'(v)H^{\top} & 0 & 0 & \mathcal{B}\omega'(v) \end{bmatrix},$$

with $\omega'(v) = \partial \omega(v)/\partial v$ and H defined in Theorem 1. The above matrix is positive definite if and only if

$$\mathcal{B}w'(v) - \omega'(v)H^{\top}R^{\mathcal{G}-1}H\omega'(v) > 0.$$

¹Following the model reduction, the fast dynamics exclusively depend on ζ . However, the two systems are generally formulated as a function of all potential slow (x) and fast (z) states, such that f(x,z) and g(x,z).

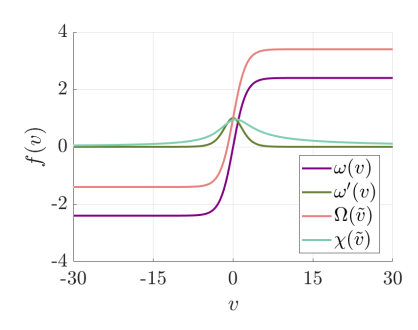


Fig. 2: Hyperbolic tangent functions

Multiplying the above condition by the inverse of $\omega'(v)$, we get that

$$\mathcal{B} > H^{\top} R^{\mathcal{G}-1} H \omega'(v).$$

Given the sigmoid nature of the monotonic (saturation) function $\omega(v)$, we notice that $0 < \omega'(v) \le \omega'_{\max}$ as visualized in Fig. 2, which implies that \mathcal{B} can be chosen to be greater than a *constant* value \mathcal{B}^* , defined as the largest eigenvalue of $H^\top R^{\mathcal{G}-1}H\omega'_{\max}$, which is indeed the condition in *Theorem* 1. If it holds, then we can bound the terms appearing in (10a)-(10b) as follows

$$-(x-\bar{x})^{\top}[\mathcal{M}_x(x)-\mathcal{M}_x(\bar{x})] \leq -\Upsilon||\tilde{x}||^2, \tag{12a}$$

$$-\tilde{y}^{\top} \mathcal{P}_{y} \tilde{y} \leq -\alpha_{y} ||\tilde{y}||^{2}, \tag{12b}$$

for some $\Upsilon>0$ and where $\alpha_y>0$ is the smallest eigenvalue of $\frac{1}{2}(\mathcal{P}_y+\mathcal{P}_y^\top)$. Under the three given bounds (11), (12a), (12b), exponential stability of both the reduced- and the boundary layer system is proven, as both $V_s(\tilde{x})$ and $W_f(\tilde{y})$ are positive definite and radially unbounded, for all $\mathcal{B}\geq\mathcal{B}^*$. The composite Lyapunov function for the *full* system is then given in (13) as a weighted sum of the reduced- and boundary layer systems' Lyapunov functions where d is the Lyapunov parameter later used to bound the value of ε .

$$\mathcal{L}(\tilde{x}, \tilde{y}) = (1 - d)V_s(\tilde{x}) + (d)W_f(\tilde{y}) \ge 0, \quad 0 < d < 1$$
 (13)

The time-derivative of the composite Lyapunov function along the trajectories of the *full* system is then

$$\dot{\mathcal{L}}(\tilde{x}, \tilde{y}) = (1 - d) \frac{\partial V_s(\tilde{x})}{\partial \tilde{x}} f(\tilde{x}, h(\tilde{x})) + \frac{d}{\epsilon} \frac{\partial W_f(\tilde{y})}{\partial \tilde{y}} g(\tilde{x}, \tilde{y} + h(\tilde{x})) + (1 - d) \frac{\partial V_s(\tilde{x})}{\partial \tilde{x}} [f(\tilde{x}, \tilde{y} + h(\tilde{x})) - f(\tilde{x}, h(\tilde{x}))] - d \frac{\partial W_f(\tilde{y})}{\partial \tilde{y}} \frac{\partial h(\tilde{x})}{\partial \tilde{x}} f(\tilde{x}, \tilde{y} + h(\tilde{x})) \leq 0.$$
(14)

The above two first terms represent the time-derivative along the reduced system, $\dot{V}_s(\tilde{x})$, and the boundary layer system, $\dot{W}_f(\tilde{y})$, respectively, and are proven ≤ 0 following the conditions in (11), (12a), (12b). The two last terms in (14) represent the *interconnection* between the slow and fast dynamics. Hence, both terms need to be bounded ≤ 0 , to conclude G.E.S. for the *full* system.

In (15) the dynamics of the reduced system in (6) is extended to include all dynamics following $\varepsilon = \tau_d$ and $\tilde{\zeta} = \tilde{y} + h(\tilde{x})$.

$$f(\tilde{x}, \tilde{y} + h(\tilde{x})) \begin{cases} Q_x \dot{\tilde{x}} = (\mathcal{J}_x - \mathcal{P}_x) \tilde{\hat{x}} + \kappa_1 \chi(\tilde{v}) \tilde{v} \\ \dot{\tau} \dot{\tilde{v}} = -\Gamma(\tilde{v}) + h \Lambda \kappa_1^\top \hat{\tilde{x}} - \beta \tilde{v} - \mathcal{K}_v K_1 \mathcal{L} \tilde{y} \end{cases}$$
(15)

For convenience, we have defined

$$\chi(\tilde{v}) \triangleq \text{bdiag}\left\{\frac{\Omega(\tilde{v}_i)}{\tilde{v}_i}\right\},\,$$

which may be interpreted as the rate of change of the positive definite function $\Omega(\tilde{v})$. Hence $\chi(\tilde{v})$ is positive definite as visualized in Fig. 2. The first interconnection term in (14) is bounded by

$$(1-d)\frac{\partial V_{s}(\tilde{x})}{\partial \tilde{x}}[f(\tilde{x}.\tilde{y}+h(\tilde{x}))-f(\tilde{x}.h(\tilde{x}))]$$

$$=-(\tilde{v}\chi(\tilde{v}))^{\top}\tau\mathcal{K}_{v}K_{1}\mathcal{L}\tilde{y}$$

$$\leq|(\tilde{v}\chi(\tilde{v}))^{\top}\tau\mathcal{K}_{v}K_{1}\mathcal{L}\tilde{y}|$$

$$\leq||\tilde{x}||\Xi_{1}||\tilde{y}||, \qquad (16)$$

where the triangular- and Frobenius norm are used with $\Xi_1 \triangleq ||\chi(\tilde{v})\tau \mathcal{K}_v K_1 \mathcal{L}||_{\mathcal{F}}$ together with the fact that $\chi(\tilde{v})$ is bounded. Subsequently, the second interconnection term in (14) is bounded as follows

$$-d\frac{\partial W_{f}(\tilde{y})}{\partial \tilde{y}}\frac{\partial h(\tilde{x})}{\partial \tilde{x}}f(\tilde{x},\tilde{y}+h(\tilde{x}))$$

$$=\tilde{y}^{\top} \begin{bmatrix} K_{2}\Lambda & 0 & 0 \end{bmatrix} \begin{bmatrix} Q_{x}^{-1}(\mathcal{J}_{x}-\mathcal{P}_{x})\tilde{\hat{x}}; \kappa_{1}\chi(\tilde{v})\tilde{v} \end{bmatrix} \tilde{x}$$

$$\leq ||\tilde{y}||\Xi_{2}||\tilde{x}||, \tag{17}$$

where $\Xi_2 \triangleq \| \begin{bmatrix} K_2\Lambda & 0 & 0 \end{bmatrix} \begin{bmatrix} \mathcal{Q}_x^{-1}(\mathcal{J}_x - \mathcal{P}_x)\tilde{x}; \kappa_1\chi(\tilde{v})\tilde{v} \end{bmatrix} \|_{\mathcal{F}}$. Hence, under the given bounds (11), (12a) (12b), (16), (17), the time-derivative of the Lyapunov function in (14) may be expressed as

$$\dot{\mathcal{L}}(\tilde{x}, \tilde{y}) \leq -(1-d)\gamma \|\tilde{x}\|^2 - \frac{d}{\varepsilon} \alpha_y \|\tilde{y}\|^2 + (1-d)\Xi_1 \|\tilde{x}\| \|\tilde{y}\| + d\Xi_2 \|\tilde{x}\| \|\tilde{y}\|, \tag{18}$$

Following the results in [26] (18) may be expressed in compact form as given below.

$$- \left[\|\tilde{x}\|^\top \|\tilde{y}\|^\top \right] \begin{bmatrix} (1-d)\gamma & -\frac{1}{2} \left((1-d)\Xi_1 - d\Xi_2 \right) \\ -\frac{1}{2} \left((1-d)\Xi_1 - d\Xi_2 \right) & d\frac{\alpha_y}{\varepsilon} \end{bmatrix} \begin{bmatrix} \|\tilde{x}\| \\ \|\tilde{y}\| \end{bmatrix}$$

Schur's complement is applied to ensure the positive definiteness of the matrix and thereby deriving an upper bound for the value of ε

$$\varepsilon < \frac{d(1-d)\gamma\alpha_y}{\frac{1}{4}[(1-d)\Xi_1 - d\Xi_2]^2}.$$

We are interested in choosing a Lyapunov parameter d that leads to the highest ε to reduce the conservativeness of the stability certificate. Following the results in [26] we define

$$d^* \triangleq \frac{\Xi_1}{(\Xi_1 + \Xi_2)} \quad \text{such that} \quad \varepsilon^* = \frac{\gamma \alpha_y}{\Xi_1 \Xi_2}.$$

Hence, the singularly perturbed system, given in (6)(7), satisfies all conditions given in Theorem 11.4 in [26] and the system in (3),(5) is globally exponentially stable as there exists a $\varepsilon^* > 0$ for all $\tau_d < \varepsilon < \varepsilon^*$.

C. Control Parameter Tuning Guidelines for Stability Guarantees

The previous section concludes that the system exponentially converges to a steady state when we impose a sufficient time-scale separation of the nested control loops–following Assumption 1, when we implement a constant leakage \mathcal{B} -as in (5d), and when the controller satisfies the G.E.S. condition: $\mathcal{B} > H^\top R^{\mathcal{G}-1}H\omega'(v)$. However, when we include the constant leakage, it becomes evident

that an elevated \mathcal{B} inhibits proportional current sharing in steady state, for both saturated and unsaturated operations–following *Lemma* 1. Hence, it is desirable to minimize the value of \mathcal{B} to ensure *almost* optimal current sharing within acceptable limits, while satisfying the G.E.S. condition and accurate time-scale separation.

Fig. 3 presents some tuning guidelines for finding an acceptable and optimal \mathcal{B} -value with associated control parameters. Given that the primary objective of the controller is to guarantee G.E.S., careful control parameter tuning is essential to ensure that the system meets the stability conditions. However, from the definition of \mathcal{B}^* , the resulting value may increase the speed of the decentralized inner loop as the associated time constant is updated to τ/\mathcal{B} when the constant leakage is implemented. Hence, an elevated \mathcal{B}^* -value may decrease the time constant such that it becomes faster than the communication; i.e., $\tau/\mathcal{B} \not\succ \tau_p, \tau_d$, which contradicts the *Assumption* 1.

From the definition of H and h in Theorem~1, the maximum eigenvalue of $H^{\top}R^{\mathcal{G}-1}H\omega'(v)$ is highly dependent on the generator resistances $(R^{\mathcal{G}})$ and integrator gain (\mathcal{K}_v) . Additionally, the positive control gain (k) and rated currents (Λ) have a smaller influence on the maximum eigenvalue. The initial (and preferable) loop in Fig. 3 relies solely on tuning the controller (\mathcal{K}_v) and k) to satisfactorily reduce the value of \mathcal{B}^* . However, if this tuning is insufficient in satisfying the stability conditions, there exists a supportive tuning approach that includes modifying some electrical parameters $(R^{\mathcal{G}})$ and $(R^{\mathcal{G}})$ to further reduce the value of $(R^{\mathcal{G}})$. The drawback of the supportive loop is that the resulting $(R^{\mathcal{G}})$ restricts the applicability, as the stability depends on electrical specifications.

The algorithms also depict that even though we obtain an acceptable \mathcal{B}^* , the value might be sub-optimal as it diminishes consensus and *almost* proportional current sharing is not achieved within an acceptable tolerance from optimality. In this case, we go back to the initial loop (or supportive loop), tuning the control parameters (and electrical parameters) to find an acceptable and optimal \mathcal{B}^* .

Remark 2. It is important to note that, given the already high-speed nature of DC systems, very fast communication rates are essential to uphold this time-scale separation. Interestingly, recent advancements in electric intelligent vehicular technology have led to the development of more reliable and faster communication protocols to enhance the safety and performance of autonomous vehicles. To deal with this growing demand for data transmission, the Controller Area Network with Flexible Data Rate (CAN-FD) communication protocol has been introduced, supporting data rates of up to 8 Mbps [28]–[30]. Although potentially limited to some (geographically-contained) applications, the CAN-FD protocol provides sufficient communication rates supporting the proposed time-scales proposed in this research.

IV. CASE STUDIES

The control framework in (2) is tested by means of time-domain simulations in MATLAB/Simulink on a 48-volt DC network admitting the dynamics in (1), powered by 4 DGs, interconnected electrically and through communication links according to the arbitrary interconnection patterns depicted in Fig. 4. The specifications of the generators, loads, and transmission lines are given in Table I, where all resistance (R) and inductance (L) values are specified in per unit (p.u) on a $(0.15\Omega,300\mu H)$ base. The control parameters; $\tau=1ms$, $\tau_d=0.1ms$ and $\tau_p=0.01ms$, are selected to

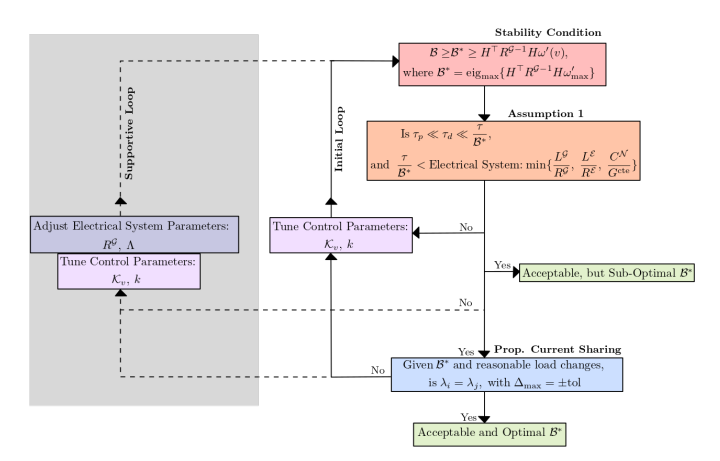


Fig. 3: Practical tuning guidelines

satisfy Assumption 1, k=10 and $\alpha=V_{\rm max}$ in the leakage function. The maximum allowed voltage deviation from the nominal voltage, $V_n=48V$, are 5%; $V_{\rm max}=1.05$ [p.u] and $V_{\rm min}=0.95$ [p.u].

The subsequent case studies aim to prove that the proposed controller, verifying the stability conditions derived in *Theorem* 1, ensures optimal operation of the DC MG in steady state, where both voltage containment and *almost* proportional current sharing are ensured following *Lemma* 1. Section III-C highlights that achieving stable operations and proportional current sharing depends on \mathcal{B} and the associated parameters $R^{\mathcal{G}}$, and \mathcal{K}_v . Accordingly, our goal is to determine a set of tuning parameter values that ensures *almost* proportional current sharing, permitting a practically acceptable $\pm 5\%$ deviation from the optimal steady state operating point.

A. Case Study 1: Control Performance of the Base-Case Scenario

Initially, we evaluate the performance of the proposed distributed control framework in [9]; i.e., without stability guarantees ($\mathcal{B}=0$), however, with the modified nonlinear leakage function in (2e)–serving as a base-case scenario depicted in Fig. 5 (a)-(c). The distributed controller is activated at t=5 s and in $t\in[10-38]$ we impose load changes increasing/decreasing the constant load currents and resistances by a minimum of 35% and a maximum of 900%. When $t\in[45,83]$, we disconnect/reconnect DG1, load 2, and the transmission line between load 3 and 4. These system events are imposed to evaluate the controllers ability to ensure voltage containment and proportionally share the currents in steady state under both minor and more extreme load variations, as well as testing the robustness and stable plug-and-play capability under various network reconfiguration events.

Fig. 5(a) illustrates that the distributed generators cooperatively reduce and increase their voltages in these events to ensure proportional current sharing—however, they are always contained within the specified limits. When the power consumption at loads 1, 2 and 3 is significantly increased ($t \in [22-35]$), DG3 and DG4 reach their saturation limits, i.e., the maximum voltage within the safe voltage range, and their respective leakage functions are activated, as given in Fig. 5 (b). Furthermore, Fig. 5(c) demonstrates that the active leakage function undermines the controllers ability to maintain proportional current sharing under these events. This is evident as the integration error fails to stabilize around zero.

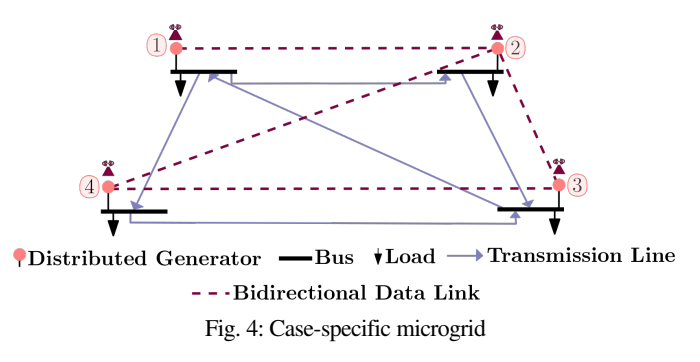


TABLE I: Parameter values for case-specific MG

Generator specifications; $i \in \mathcal{G}$									
I_i^{rated} [A]	12	4	8	8					
$R_i^{\mathcal{G}}[\text{p.u}], L_i^{\mathcal{G}}[\text{p.u}]$	0.5	0.4	0.55	0.6					
Load specifications; $k \in \mathcal{N}$									
$C_k^{\mathcal{N}}[F]$	22×10^{-3}								
$1/G_k^{\mathcal{N}}[\Omega]$	40	30	30	30					
$I_k^{\mathrm{cte}}[\mathrm{A}]$	1	1.2	0.8	1					
Transmission lines specifications; $j \in \mathcal{E}$									
$R_j^{\mathcal{E}}[\text{p.u}], L_j^{\mathcal{E}}[\text{p.u}]$] 1	2	2 1	1					

B. Case Study 2: Control Performance under Stability Constraints

In the second case study, we implement our proposed distributed controller to consistently satisfy the stability conditions given in *Theorem* 1. Thus, we include the constant leakage \mathcal{B} -function, and test the behavior of the case-specific MG under careful control parameter tuning and some electrical specifications—following the approach in Section III-C. Preliminary, when keeping the specifications given in Table I, the associated constant leakage function needs to be $\mathcal{B} \geq 349.5$ to guarantee exponential stability. However, this \mathcal{B} -value does not satisfy *Assumption* 1 as the elevated value results in a reduced time constant for the decentralized inner loop controller $(\tau/\mathcal{B}) = 2.86\mu s$, compelling it to operate on an even faster time-scale than the communication.

Unfortunately, for the initial system design, it appears infeasible to identify a set of control parameters that satisfy the required stability conditions—highlighting an important drawback of the applied time-scale separation. That being said, to investigate the applicability of the proposed method, we apply the controller to a distinct version of our case-specific system following the supportive tuning guidelines in Section III-C. More precisely, we adjust the generators base resistance up to 0.2 Ω and lowered \mathcal{K}_v to 1, resulting in $\mathcal{B}=2.54$, which aligns with the appropriate time-scales for the decentralized controller $(\tau/\mathcal{B}\!=\!0.34ms)$. Thus, the simulation results given in Fig. 5 (d)-(f) feature the control performance of the DC MG under a tuning satisfying *Theorem* 1 and *Assumption* 1. The performance of the nonzero \mathcal{B} -controller is then evaluated under the same imposed load changes and network reconfigurations as considered in the previous case study.

Fig. 5(a) illustrates that the voltages remain contained in all system events, however, never reach saturation—in contrast to the first case study—due to the continuously active \mathcal{B} -function. This behavior is further confirmed in Fig. 5(e), where the leakage function $(\rho(v))$ remains deactivated throughout the simulation. Despite this inactivated leakage, optimal proportional current sharing is not achieved in steady state as the persistently activated \mathcal{B} -function, combined with arguably some extreme load variations, contributes to a non-vanishing integration error, as shown in Fig. 5(f). This error prevents convergence to zero in

steady state and leads to a high percentage deviation from the optimal current sharing condition, given by: $\Delta = \left[\frac{(\lambda_i - \Lambda_i I_i^{\mathcal{G}})}{\lambda_i}\right]_t$, measured for each time-step t. Under the imposed load changes, the maximum deviation from optimal current sharing reaches 39%. For the network reconfiguration scenarios, the deviations are measured to 45% when DG1 is disconnected, 23% upon disconnection of load 2, and 56% under the transmission line outage between load 2 and load 4. From a performance perspective, reducing the integrator gain typically slows the rate of convergence. However, with high communication frequencies, the system maintains its rapid convergence to steady state. These results indicate that, although this case study evaluates control performance under carefully tuned values of $R^{\mathcal{G}}$ and \mathcal{K}_v , the proposed control framework performs sub-optimally. Specifically, the controller consistently guarantees global exponential stability; however, it fails to reliably enforce proportional current sharing within acceptable limits under more severe load variations.

C. Case Study 3: Control Performance under Stability Constraints for practical G.E.S.

In the third case study, we retain the parameter values from Case Study IV-B; that is, $\mathcal{B} = 2.54$ (with $\mathcal{K}_v = 1$ and $R^{\mathcal{G},\text{base}} = 0.2$). However, the system is now simulated under arguably more realistic load variations. We continue to disconnect and reconnect DG1 and the transmission line, but load 2 remains connected to preserve the presence of small load events. Since we are operating a low-voltage MG, we only allow for load changes up to 50%, and the system response is given in 5(g)-(i). Fig. 5(i) demonstrates that *almost* proportional current sharing is consistently achieved within the allowable $\pm 5\%$ tolerance, with a maximum deviation of 3.1% when we enforce load variations, and 2.1% during both the disconnection of DG1 and the transmission line outage. The voltages depicted in Fig. 5(g) remain contained and are elevated when the secondary controller is activated, as necessary to ensure proportional current sharing. Additionally, the chosen value of \mathcal{B} effectively deactivates the leakage function $(\rho(v))$, as illustrated in Fig. 5(h). The results of this case study demonstrate that the controller consistently ensures globally exponentially stable operation while steering the microgrid to a near-optimal steady state, where proportional current sharing is achieved within acceptable tolerances and voltages remain within prescribed limits. Moreover, the findings confirm the controllers robust plug-and-play capabilities, maintaining stability despite topological changes in the electrical network. These outcomes underscore the practical applicability, robustness, and scalability of the proposed distributed control scheme.

D. Case Study 4: Control Performance under Communication Delays

In the fourth case study, we simulate the case-specific DC MG under communication delays introduced in the distributed outer loop controller, while maintaining the load conditions from Case Study IV-C, including the disconnection of DG1 and the transmission line outage. The objective is to evaluate the control performance and the controllers ability to achieve consensus under realistic, assorted communication delays. Moreover, as suggested in [31], such time delays can be interpreted as a proxy for communication packet losses, thereby offering insight into the systems robustness under adverse communication conditions. In the primary scenario–depicted in Fig. 6 (a), (b), and (d)– DG2 communicates with its neighbors with a delay of

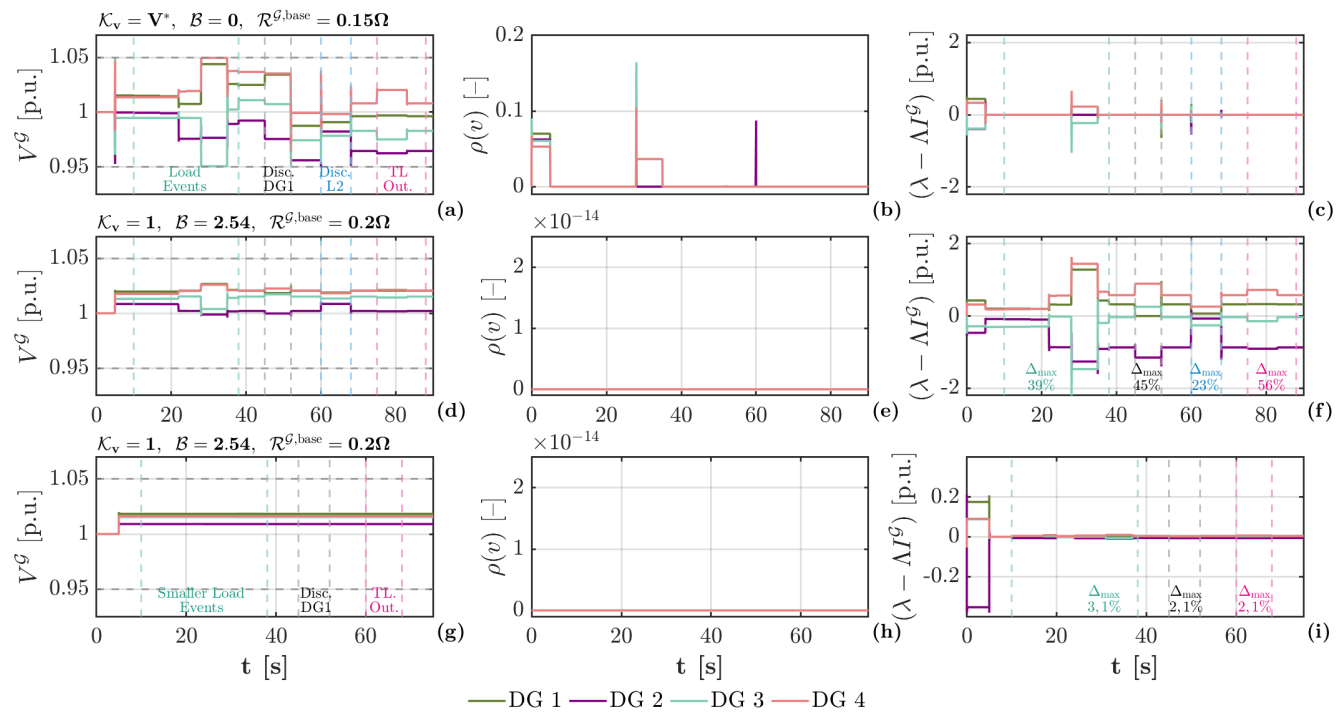


Fig. 5: Simulation results for Case Study 1 (a)-(c) (first row), Case Study 2 (d)-(f) (second row), Case Study 3 (g)-(i) (third row); (a), (d), and (g) generators voltages; (b), (e), and (h) leakage function; (c), (f), and(i) integrations errors; Imposed load changes in Case Study 1 & 2: t=5: activation of distributed controller, t=10: $Inc.G_1^{cte}45\%$, t=17: $Inc.I_1^{cte}75\%$, t=22: $Inc.G_2^{cte}500\%$ and $Inc.I_1^{cte}800\%$, t=24: $Red.I_1^{cte}35\%$, t=28: $Inc.G_3^{cte}900\%$, t=35: $Red.G_3^{cte}80\%$, t=38: $Red.I_3^{cte}90\%$; Imposed disconnections in Case Study 1&2: $t\in[45,52]$ Disc. DG1, $t\in[60,68]$ Disc. load 2, $t\in[75,83]$ Disc. TL between load 3 and 4; Imposed load changes in Case Study 3: t=5: activation of distributed controller, t=10: $Inc.I_1^{cte}50\%$, t=17: $Red.I_4^{cte}13\%$, t=20: $Red.G_3^{cte}40\%$, t=24: $Inc.G_2^{cte}5\%$, t=31: $Inc.G_3^{cte}17\%$, t=37: $Red.I_3^{cte}45\%$, t=38: $Red.G_3^{cte}7\%$; Imposed disconnections in Case Study 3: $t\in[45,52]$ Disc. DG1, $t\in[60,68]$ Disc. TL between load 3 and 4

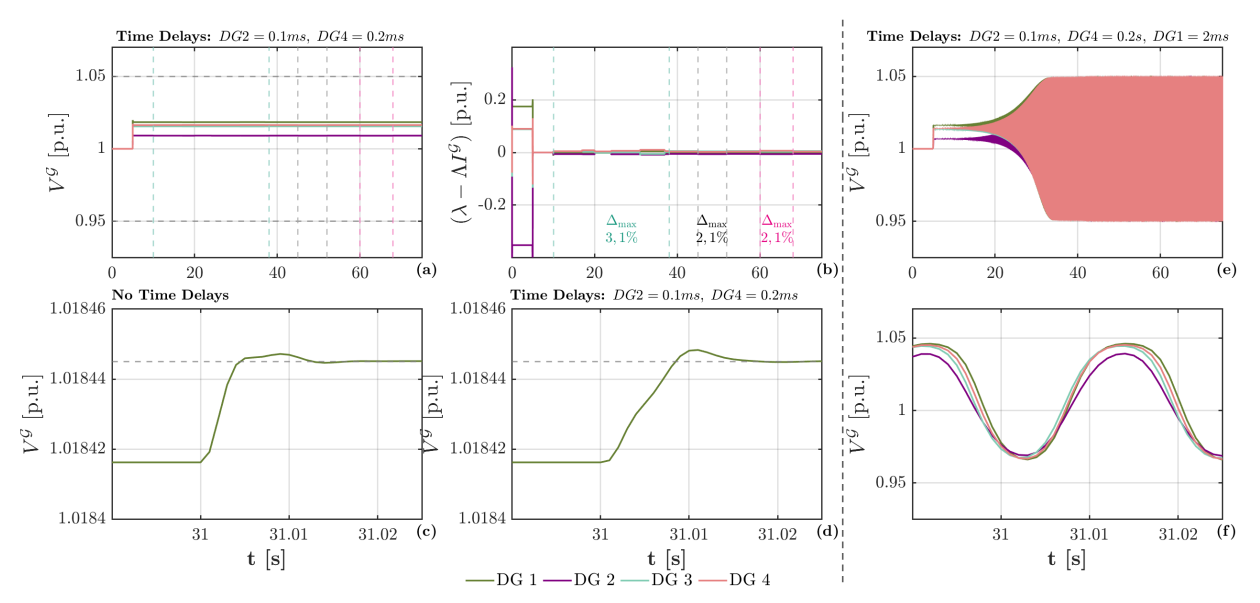


Fig. 6: Case-specific microgrid under time delays; (a)(b)(d) system response under time delays that respect the time-scale separation: (a)(d) generator voltages, (b) integration error; (c) generator voltages under normal operations; (e)(f) system response under time delays that violates the time-scale separation: (e) generator voltages, (f) integration error

0.1ms, and DG4 with a delay of 0.2ms. These delays still respect the time-scale separation necessary to guarantee G.E.S., as the communication dynamics remain significantly faster than the electrical system. As illustrated in Fig. 6(a) and (b), the system successfully converges to the same steady state values despite the imposed delays, confirming

the robustness of the control scheme. Furthermore, Fig. 6(b) highlights that the maximum deviation from optimal current sharing remains consistent with the previous case study simulated without delays—Section IV-C, thereby validating the preservation of optimality within $\pm 5\%$.

However, Fig. 6(c) and (d) indicate that the presence of communication delays leads to a slower transient response, as reflected in the rise time. We define rise time as the duration from the onset of an event to the point where the system reaches its steady state value. Comparing Fig. 6(c) and (d) reveals that, although both systems approximately stabilize at the same time, the rise time is noticeably shorter in the delay-free case. Nevertheless, the overall convergence time remains similar, likely due to other slow system dynamics unaffected by the very fast communication delays. For instance, decreasing the integrator gain \mathcal{K}_v —as per case study IV-B and IV-C—reduces the integration rate, thereby diminishing the impact of the fast communication delays and contributing to a convergence time which resembles the convergence time in the delay-free case.

Moreover, to further evaluate the stability of our system under more severe communication delays, we impose time delays that violates the time-scale assumptions necessary to guarantee G.E.S. Hence, in Fig. 6 (e)(f) DG1 communicates with its neighbors with a time delay of 2ms and DG4 with a time delay of 0.2s, while DG2 still has a time delay of 0.1ms. As depicted in the system response, it is evident that the system becomes unstable under such operations as the generator voltages stabilize to an orbit. However, notably, the voltages are always contained within a limit cycle due to the nonlinear decentralized inner loop controller.

E. Case Study 5: Small-Signal Stability Analysis

Finally, we conduct a small-signal stability analysis to determine whether a less conservative stability bound exists, thereby expanding the area of application of the results in this research. Given that large-signal stability is preserved within substantial margins – characterized by significant time-scale separation between the nested control loops – we explore the possibility of operating the system under reduced large-signal stability margins for slower communication rates. To demonstrate the impact of decreasing the communication rate and thereby reducing the time-scale separation, we plot the eigenvalues of the case-specific DC MG for a parametric sweep of the communication time constants τ_p and τ_d while keeping the constant leakage value: $\mathcal{B} = 2.54$. The resulting eigenvalues are given in Fig. 7 (a)-(b).

From Fig. 7 (a), it is evident that reducing the rate of communication brings the system closer to unstable operations as the eigenvalues tend towards positive real values. However, the eigenvalues never become positive. Therefore, from a small-signal perspective, the system is stable for all values of τ_p , τ_d .

Note that the distributed controller (dynamics given in (3e) and (3f)) relies on communication with a topology defined by the Laplacian matrix, which appears twice in the outer loop. Therefore, due to the property of the Laplacian, there will be two resulting eigenvalues very close to zero. However, with the value of \mathcal{B} , one of these zero eigenvalues (associated to the communicated λ -values) is amplified and shifted further into the left-half plane. Moreover, the zero-eigenvalue corresponding to the communicated ζ -states can be shifted further into the left-half plane by introducing an additional leakage function \mathcal{B}_{ζ} , subtracted in (3f) as $-\mathcal{B}_{\zeta}\zeta_i$. This adjustment will improve the stability margins from a small-signal perspective and for a smaller time-scale separation; however, it also moves the system further from its optimal operating point, where *almost* optimal current sharing is achieved. Hence, it is important to minimize the value of \mathcal{B}_{ζ} such that all communicating DGs agree upon a consensus value; i.e.,

TABLE II: Equilibrium for different \mathcal{B}_{ζ}

\mathcal{B}_{ζ}	λ_1	λ_2	λ_3	λ_4	ζ_1	ζ_2	ζ3	ζ_4
10	0.3505	0.3619	0.3567	0.3565	-0.0011	0.0022	-0.0005	-0.0006
1	0.3512	0.3604	0.3569	0.3567	-0.0093	0.0165	-0.0033	-0.0040
$1e^{-4}$	0.3560	0.3560	0.3560	0.3560	-0.0638	0.0584	0.0042	0.0012

 $\lambda_i = \lambda_j$, and $\zeta \approx 0$. Table II depicts the equilibrium values of the outer loop controller states λ and ζ for different tuning of \mathcal{B}_{ζ} , and, notably, the maximum allowed values is $1e^{-4}$ before hindering proportional current sharing as $\lambda_i \neq \lambda_j$. Moreover, due to the high value of \mathcal{B} , further decreasing this value will not improve the equilibrium. Hence, the eigenvalues mapped in Fig. 7(a)(b) are given for $\mathcal{B}_{\zeta} = 1e^{-4}$.

The small-signal stability assessment reinforces the findings of the large-signal stability analysis—the constant leakage (\mathcal{B}) guarantees overall stability—while enabling slower communication rates. This is further illustrated when we examine the eigenvalues of the casespecific MG for $\mathcal{B} = 0$, k = 0, and decreasing the allowable voltage range ($\Delta = 1$); i.e., without careful tuning of the control framework. The resulting eigenvalue plot-detailed in Fig. 7(c)-depicts positive real eigenvalues, and the system is unstable. Moreover, it should be noted that the eigenvalues tend towards negative real values when we further decrease the communication rates to be slower than the electrical system, even with a zero constant leakage value. This motivates a converse time-scale separation, where the communication is assumed to operate on a slower time-scale than the electrical system. Under this assumption, implementing a constant leakage to compensate for the lack of structure in the *reduced* system is no longer necessary—which is addressed in [32] and further explored in future work.

V. CONCLUSION AND FUTURE WORK

In conclusion, this paper provides a global exponential stability (G.E.S.) certificate for a *scalable* DC microgrid with a nonlinear distributed control framework originally proposed in [9] and later modified in [1]. Building upon the methodology used in [2], we apply *singular perturbation theory*, assuming that the communication dynamics operates at a faster time-scale than the electrical system. The stability guarantee relies on implementing a constant leakage function, \mathcal{B} , which, when combined with Lyapunov-based arguments, yields a final stability condition depending on the value of \mathcal{B} . This result underscores the critical importance of carefully tuning the control parameters \mathcal{B} for near-optimal operations—specifically, maintaining voltage containment and proportional current sharing within an acceptable tolerance, while satisfying the derived stability condition and time-scale assumption.

That being said, the performance of the proposed control design—and particularly its control parameter tuning—remains somewhat dependent on the specific electrical system characteristics, which may limit its general applicability across highly diverse networks. Furthermore, the theoretical large-signal stability guarantees rely on relatively fast communication rates, making the current configuration more applicable to smaller, localized systems where such communication speeds are feasible. Additionally, due to the use of the constant leakage term, practical current sharing performance is inherently restricted by the magnitude of system events, introducing a trade-off between stability and current sharing accuracy. One potential approach to mitigate this limitation is to implement an additional outer loop controller that estimates the steady state value of the decentralized control variable v^{\ast} under various system events. This

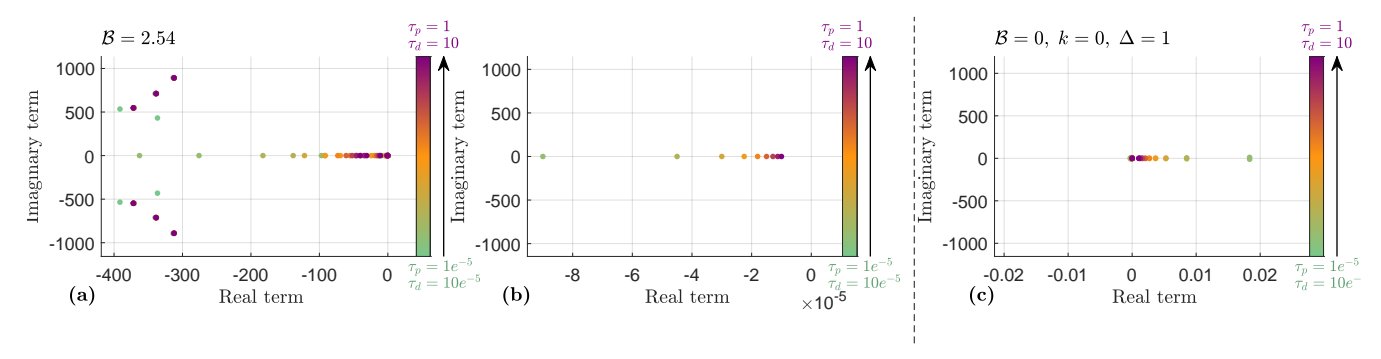


Fig. 7: Eigenvalues of the case-specific MG for a parametric sweep of τ_p , τ_d ; (a) and (b) eigenvalues under acceptable control parameters (and associated electrical specifications), (b) detailed plot around zero; (c) eigenvalues under unstable tuning conditions (detailed plot around zero)

approach would enable compensation for the effects of the leakage function \mathcal{B} , which could improve the controllers ability to maintain accurate current sharing under a wide range of network perturbations.

To complement our large-signal stability results, we conducted a small-signal stability analysis, providing practical guidelines for relaxing the time-scale separation-thus enabling operation under lower communication rates. While it is indeed possible to operate outside the large-signal tuning conditions, doing so requires additional compensatory measures, such as further time-domain simulations or eigenvalue analyses, to ensure reliable and stable system operations. Moreover, while the practical studies demonstrate stable and near-optimal operations under communication delays that are within the assumed time-scale separation, exceeding these limits forces slower outer loop dynamics, ultimately leading to system instability. Consequently, the findings of this study motivate a distinct type of stability analysis. One potential direction involves employing inverse time-scale separation-allowing communication dynamics to operate slowly with fast electrical dynamics, as suggested in [32]—which may also enhance robustness against slower communication delays.

REFERENCES

- C. Skaga et al., "Stability of a distributed controller for optimal current sharing and voltage containment in dc microgrids," *IEEE GPECOM*, 2024.
- [2] B. Abdolmaleki et al., "Distributed optimization for reactive power sharing and stability of inverter-based resources under voltage limits," *IEEE Trans. Smart Grid*, vol. 15, no. 2, pp. 1289–1303, Mar. 2024.
- [3] F. D. Kanellos, "Real-time control based on multi-agent systems for the operation of large ports as prosumer microgrids," *IEEE Access*, vol. 5, pp. 9439–9452, 06 2017.
- [4] A. A. Tavagnutti et al., "The coordinated power control of flexible dc microgrids in sustainably optimized yacht marinas," *Energies*, vol. 17, no. 2, 2024.
- [5] E. Nivolianiti et al., "Energy management of shipboard microgrids integrating energy storage systems: A review," *Renewable and Sustainable Energy Reviews*, vol. 189, p. 114012, 2024.
- [6] L. Xu et al., "A review of dc shipboard microgrids—part i: Power architectures, energy storage, and power converters," *IEEE Transactions on Power Electronics*, vol. 37, no. 5, pp. 5155–5172, 2022.
- [7] N. C. Alluraiah and P. Vijayapriya, "Optimization, design, and feasibility analysis of a grid-integrated hybrid ac/dc microgrid system for rural electrification," *IEEE Access*, vol. 11, pp. 67 013–67 029, 2023.
- [8] M. M. Kamal et al., "Optimal sizing of standalone rural microgrid for sustainable electrification with renewable energy resources," Sustainable Cities and Society, vol. 88, p. 104298, 2023.
- [9] B. Abdolmaleki and G. Bergna-Diaz, "A nonlinear control framework for optimal load-sharing and voltage containment in dc networks," *IEEE Trans. Power Syst.*, vol. 38, no. 1, pp. 976–979, 2023.
- [10] S.Sahoo et al., "On detection of false data in cooperative dc microgrids-a discordant element approach," *IEEE Transactions on Industrial Electronics*, vol. 67, no. 8, pp. 6562–6571, 2020.
- vol. 67, no. 8, pp. 6562–6571, 2020.
 [11] C. Skaga and G. Bergna-Diaz, "Cyber-attack resilient dc microgrids under distributed control: An energy perspective," 2024 European Control Conference (ECC), 2024.

- [12] D. Pullaguram and S. Sahoo, "Cyber security in multi-agent microgrids," in Cyber Security for Microgrids, D. Pullaguram and S. Subham, Eds. Stevenage: The Institution of Engineering and Technology, 2022, pp. 105–125.
- [13] M. Cucuzzella et al., "A robust consensus algorithm for current sharing and voltage regulation in dc microgrids," *IEEE Transaction on Control System Technology*, vol. 27, no. 4, pp. 1583–1595, 2019.
- [14] A. Cecilia et al., "Detection and mitigation of false data in cooperative de microgrids with unknown constant power loads," *IEEE Transactions on Power Electronics*, vol. 36, no. 8, pp. 9565–9577, 2021.
- [15] M. Sadabadi et al., "Stability-oriented design of cyberattack-resilient controllers for cooperative dc microgrids," *IEEE Transactions on Power Electronics*, vol. 37, no. 2, pp. 1310–1321, 2022.
- [16] M. Kabalan et al., "Large signal lyapunov-based stability studies in microgrids: A review," IEEE Transactions on Smart Grid, vol. 8, no. 5, pp. 2287–2295, 2017.
- [17] S. M. Ashabani and Y. A. I. Mohamed, "A flexible control strategy for grid-connected and islanded microgrids with enhanced stability using nonlinear microgrid stabilizer," *IEEE Transactions on Smart Grid*, vol. 3, no. 3, pp. 1291–1301, 2012.
- [18] J. Zhao and F. Dörfler, "Distributed control and optimization in dc microgrids," Automatica, vol. 61, pp. 18–26, 2015.
- [19] C. D. Persis et al., "A power consensus algorithm for dc microgrids," Automatica, vol. 89, pp. 364–375, 2018.
- [20] V. Nasirian et al., "Distributed cooperative control of dc microgrids," IEEE Transactions on Power Electonics, vol. 30, no. 4, pp. 2288–2303, 2015.
- [21] S. Sahoo et al., "A containment based distributed finite-time controller for bounded voltage regulation & proportionate current sharing in dc microgrids," Applied Energy, vol. 228, pp. 2526–2538, 2018.
- [22] V. Nasirian et al., "Distributed cooperative control of dc microgrids," IEEE Trans. Power Electron., vol. 30, no. 4, pp. 2288–2303, 2015.
- [23] S. Trip et al., "Distributed averaging control for voltage regulation and current sharing in dc microgrids," *IEEE Control Syst. Lett.*, vol. 3, no. 1, pp. 174–179, 2019
- [24] B.Fan et al., "A consensus-based algorithm for power sharing and voltage regulation in dc microgrids," *IEEE Trans. Ind. Informat.*, vol. 16, no. 6, pp. 3987–3996, 2020.
- [25] M. Cucuzzella et al., "A robust consensus algorithm for current sharing and voltage regulation in dc microgrids," *IEEE Transactions on Control System Technology*, vol. 27, no. 4, pp. 1583–1595, 2019.
- [26] H. K. Khalil, Nonlinear systems, 3rd ed. Prentice Hall, 2002.
- [27] B. Abdolmaleki and G. Bergna-Diaz, "Distributed control and optimization of dc microgrids: A port-hamiltonian approach," *IEEE Access*, vol. 10, pp. 64 222–64 233, june 2022.
- [28] H. Kim et al., "In-vehicle network average response time analysis for can-fd and automotive ethernet," *IEEE Transactions on Vehicular Technology*, vol. 72, no. 6, pp. 6916–6932, 06 2023.
- 29] S. Kang et al., "Controller area network with flexible data rate transmitter design with low electromagnetic emission," *IEEE Transactions on Vehicular Technology*, vol. 67, no. 8, pp. 7290–7298, 08 2018.
- [30] R. de Andrade et al., "Security architecture for automotive communication networks with can fd," Computers & Security, vol. 129, p. 103203, 2023.
- [31] Y. Yu et al., "Coordinated distributed predictive control for voltage regulation of dc microgrids with communication delays and data loss," *IEEE Transactions* on Smart Grid, vol. 14, no. 3, pp. 1708–1722, 2023.
- [32] C. Skaga and G. Bergna-Diaz, "A distributed control framework with scalable stability guarantees for dc current sharing under voltage limits," *IEEE SEST*, 2024.